Journal of Solid State Electrochemistry
https://doi.org/10.1007/s10008-026-06538-8

ORIGINAL PAPER

Inkjet-printed Pt/C materials on CuS photocathodes for photoelectrochemical water splitting

Moisés A. de Araújo[1] · Carlos André G. Bezerra[1] · Germano Tremiliosi-Filho[1] · Edson A. Ticianelli[1]

Received: 9 July 2025 / Revised: 13 January 2026 / Accepted: 7 February 2026

Abstract

Copper(II) sulphide (CuS) exhibits suitable optical properties for photoelectrochemical (PEC) H_2 generation, a non-polluting energy carrier; however, the PEC performance of this material is still unsatisfactory. In this work, we aimed to improve PEC H_2 generation via modifying the surface of CuS films with Pt/C materials deposited using a low-cost commercial inkjet printer (a conventional desktop printer). The inkjet deposition approach enabled deposition of ultra-low Pt loadings (range of 0.00036–0.0096 mg Pt cm^{-2}), representing high Pt utilisation. The presence of Pt/C on CuS films delivered a considerable cathodic photocurrent density of (-3.17 ± 0.56) mA cm^{-2} at 0 V vs. RHE for the hydrogen evolution reaction (HER), which is 7.93 times higher than that of the bare CuS film. Additionally, a positive onset potential under illumination for the HER was observed for the CuS-Pt/C films (up to approximately 0.025 V vs. RHE) compared to that of the bare CuS film (ca. −0.013 V vs. RHE), indicating co-catalytic contribution of the Pt in the Pt/C materials for the improvement of the HER. Electrochemical impedance measurements revealed a 2.1-fold reduction in charge transfer resistance of CuS-Pt/C films compared to bare CuS films. This indicates that the enhanced PEC H_2 generation is associated with the facilitation of photogenerated electrons transfer at the photocathode|electrolyte interface for the occurrence of the HER. In terms of PEC stability, the cathodic photocurrent density of the CuS-Pt/C film at −0.04 V vs. RHE remained steady for 20 min during the PEC experiment; however, a considerable decrease was observed for longer times, which is attributed to the photoelectrochemical decomposition of CuS. A similar stability trend was observed for the amount of H_2 generated by the CuS-Pt/C film at −0.04 V vs. RHE under illumination.

Keywords Inkjet printer · Copper(II) sulfide · Solar water splitting · Green hydrogen · Platinum co-catalyst

Introduction

The ongoing increase in global warming, caused by the uncompensated emissions of greenhouse gases in the Earth's atmosphere [1, 2], has been a growing concern. A significant contributor to this effect is the anthropogenic carbon dioxide emissions resulting from the combustion of fossil fuels for human daily life activities [3]. Owing to this environmental issue and the non-renewable nature of fossil fuels, searching for clean and sustainable energy resources has been in demand [4, 5]. Among the alternative energy sources, hydrogen gas (H_2) stands out as a promising energy carrier due to its high energy yield (ca. 122 kJ g^{-1}), which is 2.75 times higher compared to that of hydrocarbon fuels, and mainly its environmentally friendly combustion (i.e., it only generates water vapour) [6]. Currently, the main industrial method for H_2 production is via fossil fuels, namely, steam reforming natural gas, which, besides being unsustainable, produces H_2 contaminated with different hydrocarbons [7, 8]. Another possible way to obtain H_2 is via water electrolysis, which is potentially a more sustainable approach, producing high-purity H_2 and having the advantage of using water as a raw material [9].

From a thermodynamic point of view, the electrochemical cell voltage (ΔU) for the overall water splitting process is −1.229 V, but due to energetic and kinetic aspects, this process requires a high overvoltage to drive this reaction [10].

✉ Moisés A. de Araújo
moisesaaraujo@usp.br

✉ Edson A. Ticianelli
edsont@iqsc.usp.br

[1] Instituto de Química de São Carlos, Universidade de São Paulo, Avenida Trabalhador Sancarlense, 400, São Carlos, São Paulo 13566-590, Brazil

Published online: 20 March 2026

This translates into high production costs, which, from an economic perspective, limit electrolysis from becoming the mainstream method for H_2 production [11]. Such a problem can be circumvented by using semiconductor materials as photoelectrodes in photoelectrochemical (PEC) cells, which can benefit from their photoactivity of harvesting sunlight to reduce the overpotential/overvoltage of water electrolysis [12–14]. The application of semiconductor materials to perform water electrolysis at lower overpotential was first demonstrated in 1972 by Fujishima and Honda [15], who employed TiO_2 as a photoelectrode to drive water splitting at 0.5 V vs. reversible hydrogen electrode (RHE) and under illumination. Despite being an abundant, inexpensive, and non-toxic material, TiO_2 has a wide bandgap energy (E_g), namely, 3.2 eV for the anatase phase [16], which favours photon energy absorption only in the ultraviolet region (it corresponds to less than 5% of the solar spectrum that reaches the earth's surface).

Since the discovery of the photoelectroactivity of TiO_2, a wide variety of semiconductor materials have been investigated in the context of light-driven water splitting, in which different materials have shown promising results, such as oxide- [17, 18], selenide- [19], and sulphide-based [19, 20] semiconductor materials. Among the sulphide-based materials, copper(II) sulphide (CuS) has been considered a promising candidate for light-driven water splitting due to its suitable optoelectronic characteristics, such as a narrow E_g of 1.6–2.2 eV [21], which enables the absorption of light in the visible range of the solar spectrum. CuS can also favour light absorption in the near-infrared region due to the localised surface plasmon resonance effect of this semiconductor [22, 23]. Still concerning the E_g of CuS, the variation of E_g values for CuS arises due to the formation of different morphologies (i.e., changes of shape and particle size) [22]. CuS can also be employed as a photocathode in PEC cells, as this material is a p-type semiconductor and has a proper conduction band edge potential (E_{cb}) to drive the hydrogen evolution reaction (HER), i.e., to reduce hydronium (H_3O^+) to H_2 molecules, under illumination [24]. CuS is also known to be made up of earth-abundant elements and is a low-toxicity material [25].

Albeit CuS features desired optoelectronic properties for H_2 production from solar-driven water splitting, the rapid recombination of the photogenerated electron-hole pairs in this material stands, however, as one of the drawbacks to further advance towards a practical application [26]. This issue can be minimised via, e.g., combining CuS with other semiconductor materials to form a heterojunction or a heterostructure, such as CuS/NiO [27], ZnO/CuS [28], and CuS/TiO_2/CdS [29]. Deposition of noble metals on the surface of CuS films is another way to suppress the electron-hole recombination process and consequently improve photoelectrocatalytic activity for the HER. Regarding this strategy, Dubale et al. [30] synthesised Cu_2O/CuO electrodes by electrodeposition followed by an annealing treatment of this heterostructure to superficially modify with CuS via successive ion layer adsorption and reaction. Then the surface of the Cu_2O/CuO/CuS was decorated with Pt by using a sputtering technique. The Cu_2O/CuO/CuS/Pt films provided a photocurrent density for the HER of −5.7 mA cm^{-2} at 0 V vs. RHE, which was 2.6 and 1.1 times greater than that of the Cu_2O/CuO and Cu_2O/CuO/CuS films, respectively. Furthermore, the Cu_2O/CuO/CuS/Pt films were able to retain 92% of their initial cathodic photocurrent density after 1 h of the experiment, whereas the value obtained for Cu_2O/CuO the value was only 56%. The improvement of PEC performance for the Cu_2O/CuO/CuS/Pt films was assigned to the better kinetics in the photogenerated electron transfer process at the photoelectrode|electrolyte interface, as suggested by electrochemical impedance spectroscopy (EIS) measurements. This improvement in the charge transfer process simultaneously decreased electron-hole recombination and photocorrosion of the Cu_2O/CuO/CuS films.

Despite these promising results, the deposition of Pt via sputtering has the disadvantage of high cost, which is a bottleneck in the scaling up of the deposition process. Alternatively, Pt can be deposited via solution-processed methodologies, for example, photoelectrodeposition [31], drop casting [32], or using the inkjet printing method [33]. Among these different approaches, the inkjet printing method is a simple, inexpensive, scalable and low-waste technique that allows printing micron-scale patterning and deposition of thin films with highly homogeneous composition [34]. Moreover, inkjet printing enables deposition of low Pt loadings, which favours high Pt-utilisation (i.e., to have high electrocatalytic activity with a minimum amount of Pt) that enables decreasing the cost of Pt-modified electrodes [35].

The inkjet printing method has often been applied for deposition of low loadings of Pt/C on gas diffusion layer (GDL), which has been used to construct membrane electrode assembly (MEA) for polymer-electrolyte-membrane fuel cells (PEMFC) application [36–39]. In this context, Taylor et al. [38] used a commercial thermal inkjet printer to deposit different loadings of Pt/C material on GDL and Nafion® membranes for making MEA to be applied in PEMFC. The authors have shown high Pt utilisation for the MEA having inkjet-printed Pt/C with ultra-low catalyst loading (0.021 mg Pt cm^{-2}) compared to the MEA containing the catalyst deposited by the conventional screen-printing method. In another study, Bezerra et al. [36] employed a low-cost commercially available inkjet printer to deposit Pt/C with low Pt loading (0.1 mg Pt cm^{-2}) on GDE and Nafion® membrane. It was found that the fuel cell

performance was proportional to the number of catalyst layers deposited on the GDE and inversely proportional to the number of layers deposited on the Nafion® membrane. This behaviour was associated with the better dispersion of the inkjet-printed Pt/C materials on the GDE, as the GDE has a high surface area due to its porous structure, favouring a larger three-dimensional surface area containing the catalyst. Regarding the surface modification of CuS films with inkjet-printed Pt/C materials for H_2 generation via photoelectrochemical water splitting, as far as we are aware, this approach has not been performed yet.

In this work, we demonstrated that a low-cost inkjet printing method can be efficiently used to deposit Pt/C materials with ultra-low Pt loading on CuS films. Furthermore, we investigated the influence of Pt loading on the PEC performance of the CuS films superficially modified with the inkjet-printed Pt/C materials (CuS-Pt/C). The physical characterisation of the Pt/C inks, and the optical, physical and chemical properties of the CuS-Pt/C films are also discussed.

Experimental section

Chemical reagents

Chemical reagents were of analytical grade and were used without additional purification. The main chemicals used in this work were: ethylenediaminetetraacetic acid disodium (Na_2EDTA) salt dihydrate ($C_{10}H_{14}N_2Na_2O_8{\cdot}2H_2O$, Neon, ≥ 99.0%), copper(II) sulphate ($CuSO_4$, Sigma-Aldrich, ≥ 99%), sodium thiosulphate pentahydrate ($Na_2S_2O_3{\cdot}5H_2O$, Sigma-Aldrich, ≥ 99.5%), elemental sulphur powder (S, Sigma-Aldrich), 30 wt%, 50 wt%, or 80 wt% platinum on Vulcan XC-72 (Pt/C, E-Tek), Nafion ionomer (Ion Power, LQ-1105 1100 EW 5 wt%), propan-1-ol (C_3H_8O, J.T. Baker, 99.9%), propane-1,2-diol ($C_3H_8O_2$, Sigma-Aldrich, ≥ 99.5%), and sulphuric acid (H_2SO_4, Merck, 96%). The aqueous solutions were prepared with ultra-purified water (resistivity of 18.2 MΩ cm) taken from a Milli-Q® system.

Synthesis of CuS films

CuS films were prepared by electrodeposition of Cu with a subsequent sulphurisation process. The electrodeposition was performed in a conventional three-electrode cell, and the working electrode (WE), where the films were electrodeposited, was a glass substrate coated with a fluorine-doped tin oxide (FTO) layer (Sigma-Aldrich, surface resistivity of ≈ approximately 7 Ω/sq), which had been previously cleaned and hydrophilized, as reported previously [40]. The counter electrode (CE) was a graphite plate, and the reference electrode (RE) was an $Ag/AgCl/Cl^-_{(sat.\ KCl)}$. All the potential values in this study were given relative to the $Ag/AgCl/Cl^-_{(sat.\ KCl)}$ electrode (unless the RHE is indicated). The distance between the WE and the CE was ca. 1.2 cm, and the geometric area of the WE and the CE were 0.52–0.92 and 1.65 cm^2, respectively. The electrodeposition bath was a freshly made solution comprised of 30 mmol L^{-1} $CuSO_4$ and 90 mmol L^{-1} $Na_2S_2O_3$ dissolved in 0.1 mol L^{-1} Na_2EDTA at pH 10 (pH adjusted with diluted NaOH), which was the supporting electrolyte and complexing agent. Before every experiment, the electrodeposition bath was deaerated with N_2 for approximately 1 h to remove dissolved O_2. The films were electrodeposited potentiostatically at −0.95 V vs. $Ag/AgCl/Cl^-_{(sat.\ KCl)}$ (corresponding approximately to the c_2 peak potential of the cyclic voltammogram of the electrodeposition bath, see Fig. S1), and the electrodeposition was ceased once a charge density of −1.4 C cm^{-2} was reached. All these electrochemical experiments were recorded using a potentiostat/galvanostat (Autolab PGSTAT30) running with Nova software (version 2.1.4).

Since the as-electrodeposited films were S-poor (atomic S percentage was ca. 1.5%, as shown in Fig. S2), the as-electrodeposited films were subjected to sulphurisation at 300 °C for 1 h under sublimated S atmosphere and argon (Ar) flux. The heating rate was 10 °C min^{-1}, and the cooling condition was carried out naturally to room temperature. As depicted in Fig. 1, the sulphurisation system consisted of a cylindrical glass partially covered by adjoining it with another cylindrical glass. Inside this system, there were electrodeposited Cu films and 0.1 g of elemental S powder, which served as the sulphide source. This partially closed cylindrical glass was placed in a furnace glass tube for the sulphurisation process. Before the sulphurisation, the system underwent three sequential vacuum pump cycles, i.e., each cycle consisting of vacuuming the system for 1 min and then filling it with Ar for 1 min.

Formulation of Pt/C inks and printing on CuS films

The Pt/C inks containing different Pt loadings (i.e., 30, 50, and 80 wt% Pt in Pt/C) were formulated according to the procedure reported in previous work [37]. Briefly for each Pt loading condition (i.e., 30, 50, and 80 wt% Pt in Pt/C), 0.0375 g of commercial Pt/C (corresponding to 0.01, 0.02 and 0.03 g of Pt, respectively) was dispersed in a solution comprised of 0.1875 g of Nafion ionomer (4.24 wt% of total), 3.1897 g of propan-1-ol (72.1 wt% of total), and 1.0097 g of propane-1,2-diol (22.8 wt% of total). The preparation procedure consisted initially of mixing the propan-1-ol and propane-1,2-diol under magnetic stirring for 15 min, then the Pt/C catalyst and the Nafion ionomer were added sequentially. This dispersion was further mixed under

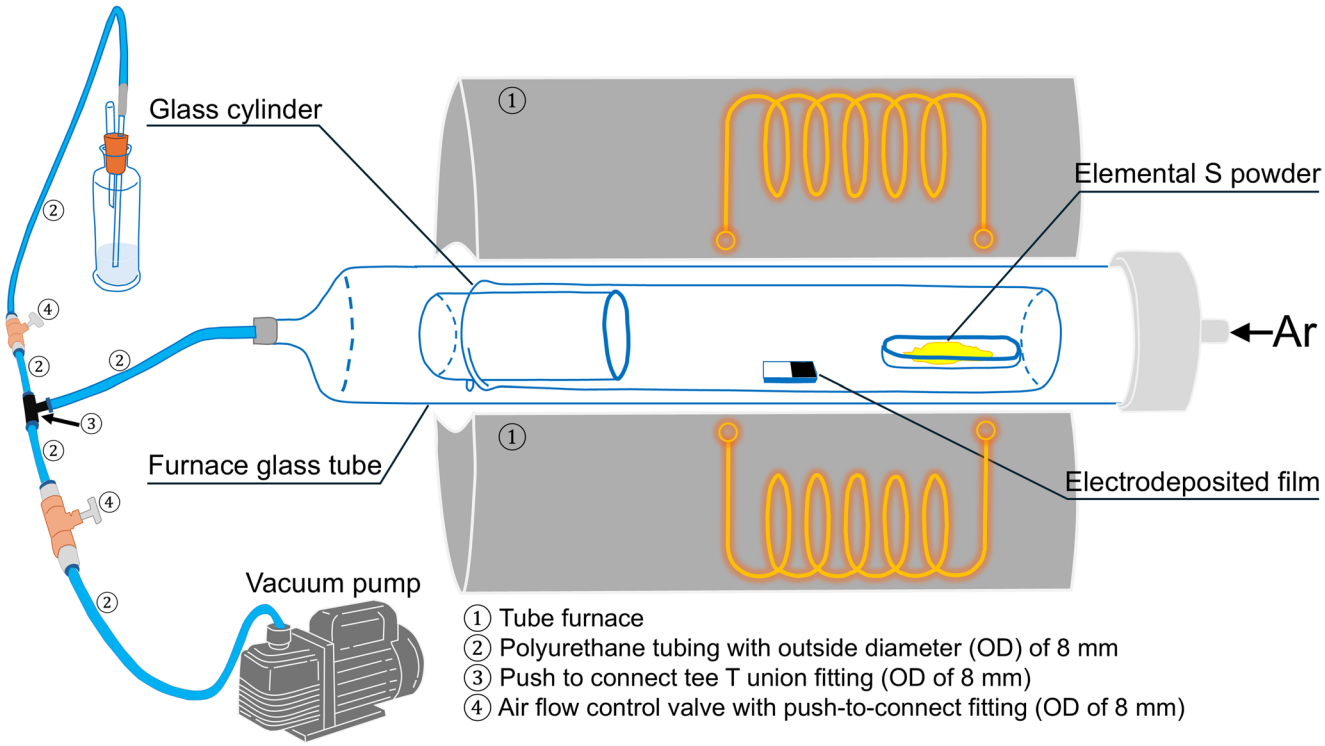

Fig. 1 Sulphurisation set-up

an ultrasonic bath for 15 min, then in an ultrasonic processor for 15 min (Acil & Weber,750 W, 20% amplitude, 3 s pulse on and 2 s pulse off). During sonication in the ultrasonic processor, the temperature of the dispersion was kept relatively constant by immersing the ink container in an ice bath. Finally, after sonication, the ink was magnetically stirred for 12 h.

Regarding the printing process, the Pt/C inks featuring different Pt loadings were printed on the CuS photoelectrodes using a commercial desktop inkjet printer (Epson EcoTank L805) having micro piezo printheads for ejection of the inks, as described previously [37]. Before printing, the Pt/C inks were filtered with a 450 nm nylon membrane syringe filter and then injected directly into an empty and clean cartridge. The CuS photoelectrode was affixed onto the compact disc (CD) printing tray, and then one layer of Pt/C ink was printed on it. The as-printed Pt/C layer over the CuS films was subsequently dried at 200 °C for 30 min with a heating rate of 10 °C min^{-1} and under Ar flux. The Inkscape software (version 1.0) was used to design the printed pattern on the CuS films, namely, a rectangle with dimensions of 2.35 cm × 1.55 cm, and we chose these dimensions for the printed pattern to guarantee that Pt/C ink was printed on the whole area of the CuS film, whose maximum dimensions were approximately 1 cm × 0.9 cm. The CuS films, having a printed Pt/C layer on their surface with Pt loadings of 30, 50, and 80 wt%, were labelled as CuS-Pt/C(30), CuS-Pt/C(50), and CuS-Pt/C(80), respectively. Based on previous work for a Pt/C(50) electrode prepared employing the same printer and procedure, the estimated Pt load is 0.006 mg Pt cm^{-2} for one printed layer [37]. Herein, the estimated Pt loads are 0.0036 and 0.0096 mg cm^{-2} for one printed layer of Pt/C(30) and Pt/C(80), respectively.

Characterisation of CuS and CuS-Pt/C films, and Pt/C inks

The characterisation of the crystal phase formation of the films was carried out on an X-ray diffractometer (Bruker D8 Advance) equipped with a copper anode (Cu $K\alpha_1$ radiation of 1.5418 Å) for the generation of the X-ray beam, which was operated at 40 kV and 40 mA. The diffractograms were obtained at a scan speed of 3° min^{-1} and a step of 0.02°. The diffraction peaks indexing was handled with the Crystallographica Search-Match software (version 2, 1, 1, 1) [41]. Additional structural characterisations of the films were performed on a Raman micro-spectrometer (Horiba LabRam HR Evolution) having a laser with a wavelength of 473 nm. For morphology analyses of the films, a field emission scanning electron microscope (FE-SEM, Jeol JSM-7200 F) was employed, and the voltage employed was 15.0 kV. The films' chemical composition assessment was also performed using FE-SEM, which contained an energy-dispersive X-ray spectrometer (Bruker Xflash 6|60 detector). Further

chemical analyses were performed with an X-ray photoelectron spectrophotometer (Scienta Omicron), and the excitation source was a monochromatic Al *Kα* radiation (1486.7 eV). All the high-resolution spectra were collected with an energy step of 0.05 eV at a pass energy of 30 eV. Aiming to correct/minimise the surface charging of the films, the binding energy scale of all the spectra was calibrated relative to the C 1s peak at 284.8 eV. All data analyses of the spectra were performed using the CasaXPS software (version 2.3.24PR1.0) [42]. The optical characterisation of the films was conducted on an ultraviolet-visible (UV-vis) spectrophotometer (Shimadzu UV-2600) containing an integrating sphere. The diffuse reflectance spectra and Eqs. 1 and 2 were used to obtain the Tauc plots, employed to estimate the optical E_g of the films [43].

$$f(R) = \frac{\alpha}{s} = \frac{(1-R)^2}{2R}, \tag{1}$$

$$[f(R)\,h\nu\,]^{n} = A(h\nu - E_g), \tag{2}$$

where $f(R)$ is the Kubelka-Munk function, α is the absorption coefficient, s is the scattering coefficient, which was assumed to be wavelength independent and that means $f(R)$ can be used instead of α [43], R is the absolute reflectance at a given $h\nu$ value, h is the Planck constant (6.626×10^{-34} J s), ν is the photon's electromagnetic wave frequency, A is a constant of proportionality, and n can have values of 2, 1/2, 2/3, or 1/3 corresponding to direct (allowed), indirect (allowed), direct (forbidden), and indirect (forbidden) transitions, respectively.

Regarding the characterisation of the Pt/C inks, surface tension (γ) measurements of the inks were carried out on a goniometer (KSV CAM 200) using the pendant drop method. The γ of the inks was estimated by utilising the CAM2008 software, and for that, the density of the Pt/C inks featuring different Pt loadings, which were approximately 0.83 g mL^{-1}, was provided to this software.

Photoelectrochemical characterisation of CuS and CuS-Pt/C films

To assess the PEC performance of the films, linear sweep voltammetry (LSV) curves were recorded in the dark and under a solar simulator (Sciencetech LH-EF-300X with a Xe arc lamp and irradiance of 100 mW cm^{-2} on the photoelectrodes' surface). The LSVs were scanned from −0.01 to −0.3 V vs. Ag/AgCl/$Cl^-_{(sat.\ KCl)}$ (from 0.24 to −0.06 V vs. RHE) at a scan rate of 50 mV s^{-1}. To further characterise the films, Mott-Schottky plots were used to estimate the flat-band potential (E_{fb}) and to determine the conductivity type of the photoelectrodes. For this experiment, a frequency of 1 kHz (sine wave) having an amplitude of 10 mV_{top} was applied, and the applied potential was from 0.20 to −0.05 V vs. Ag/AgCl/$Cl^-_{(sat.\ KCl)}$ (from 0.44 to 0.19 V vs. RHE), corresponding to 15 applied potential values. Before running the Mott-Schottky experiments, the films were cycled uninterruptedly with 50 cyclic voltammetries (from 0.20 V to −0.05 V vs. Ag/AgCl/$Cl^-_{(sat.\ KCl)}$ and a scan rate of 50 mV s^{-1}) for the sake of removing any impurity that could have been eventually adsorbed on the films' surface. Additional characterisation of the films was achieved via EIS, which was conducted under a solar simulator (the irradiance at the photoelectrodes was 100 mW cm^{-2}) and the films were polarised at −0.24 V vs. Ag/AgCl/$Cl^-_{(sat.\ KCl)}$ (0 V vs. RHE). The applied frequency range was from 100 kHz to 100 mHz (sine wave), and the amplitude was 10 mV_{RMS}. The number of frequencies was 10 frequencies per decade, and the frequency step type was points per decade. It was employed 5 sine waves (i.e., 5 superimposed frequencies) in the low frequency range (from 1 Hz to 100 mHz), and for the rest of the frequency range (from 100 kHz to 1 Hz), 1 sine wave (i.e., one single frequency applied at a time) was used. Before the impedance measurements, the photoelectrodes were polarised at −0.24 V vs. Ag/AgCl/$Cl^-_{(sat.\ KCl)}$ (0 V vs. RHE) for 60 s under a solar simulator to reach a steady-state condition. The impedance spectra were fitted with an equivalent electrical circuit by means of Zview software (version 3.1c). The PEC H_2 generated by the films at −0.04 V vs. RHE and under solar simulator (irradiance on the photoelectrode's surface corresponded to 3 suns) was measured using gas chromatography. H_2 was collected from the headspace of the sealed cell every 30 min over 3 h of the PEC experiment and injected directly into the gas chromatograph.

All these experiments were conducted on a potentiostat/galvanostat (Autolab PGSTAT30) controlled by Nova software (version 2.1.4) and using a three-electrode cell with a quartz window (cf. Figure S3). The WE were the CuS and CuS-Pt/C films (geometric area of 0.52–0.92 cm^2), and the RE and CE were an Ag/AgCl/$Cl^-_{(sat.\ KCl)}$ and a Pt plate, respectively. It was employed as the electrolyte, a N_2-saturated solution comprising 1 mol L^{-1} H_2SO_4 at a pH of 0.72 (as measured). The potential values recorded against the RE of Ag/AgCl/$Cl^-_{(sat.\ KCl)}$ were converted to potential values relative to the RHE via employing Eq. 3 [44].

$$E(\text{vs. RHE}) = E\left(\text{vs. Ag/AgCl/Cl}^-_{(\text{sat. KCl})}\right) + E_{\text{ref.}} + \text{pH}0.059, \tag{3}$$

where E(vs. RHE) is the converted applied potential relative to the RHE, E(vs. Ag/AgCl/$Cl^-_{(sat.\ KCl)}$) is the experimentally measured applied potential relative to the Ag/AgCl/$Cl^-_{(sat.\ KCl)}$, $E_{ref.}$ is the potential of the RE Ag/AgCl/$Cl^-_{(sat.\ KCl)}$ (0.1976 V vs. standard hydrogen electrode at

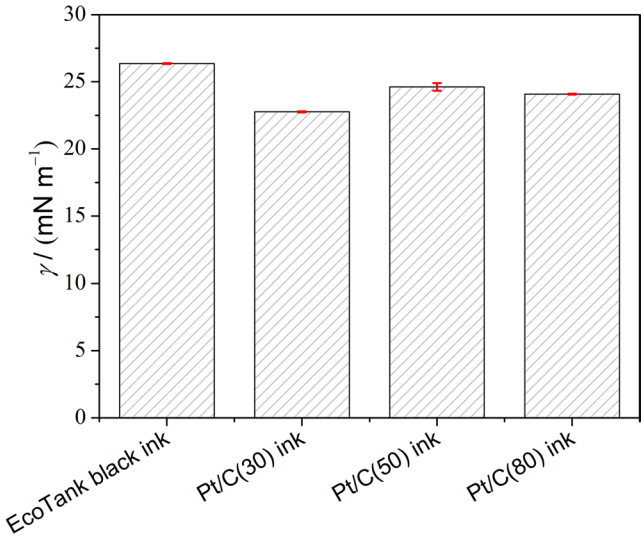

Fig. 2 Surface tension (γ) values for the commercial ink (i.e., EcoTank black ink) and the Pt/C inks with different Pt loadings

25 °C [45]), and pH is the hydrogenionic potential of the employed electrolyte (0.72).

Results and discussion

To be printed properly using an inkjet printer, the ink must have suitable physical properties, such as viscosity (η) and surface tension (γ), which are the two main parameters controlling the ink ejection from the printhead nozzles [46]. Considering this and that we used a commercial Epson inkjet printer, we initially measured the η and γ of the printer's commercial ink, then formulated Pt/C inks with similar physical properties. For this study, we specifically characterised the commercial Epson black ink, known as EcoTank black ink, as we intended to use only the ink cartridge of this colour. Regarding the physical characterisation of the EcoTank black ink, this ink was nearly Newtonian, and the η and γ were 3.6 cP at 637.5 s^{-1} (cf. Figure S4) and (26.4 ± 0.03) mN m^{-1} (see Fig. 2), respectively. For the Pt/C inks, it was shown in a previous work [37] that the Pt/C(50) ink exhibits nearly Newtonian behaviour and has a η of 3.2 cP at 675 s^{-1} and γ of 29.2 mN m^{-1}, which are fairly similar to the values for the reference ink, i.e., the EcoTank black ink, thus indicating the suitability of the Pt/C(50) ink for inkjet printing. Based on this initial work [37], we observed that the γ values for the Pt/C inks with different Pt loadings (i.e., 30, 50, and 80 wt% Pt in Pt/C) are all very close to that of the EcoTank black ink (cf. Figure 2), suggesting these inks are appropriate for use in an inkjet printer.

One layer of each Pt/C ink was then printed over the CuS films, and these superficially modified films were physically, chemically, and photoelectrochemically characterised. Before delving into the characterisation analyses, it is important to note that the CuS films exhibited a black colour (see Fig. 3a), which is consistent with other studies [47]. Printing Pt/C layer over the CuS film did not modify the appearance of the films (cf. Figure 3a), and that is probably due to the presence of only one layer. The crystalline phase characterisation of the bare CuS film and the CuS-Pt/C films was assessed via X-ray diffraction (XRD) patterns, as shown in Fig. 3b. All the diffraction peaks not labelled with hashes (#) in the diffractograms of both, bare CuS and CuS-Pt/C films were attributed to the CuS phase, which has a hexagonal crystalline structure of P63/*mmc* (no. 194) space group, as indicated by comparison with the Powder Diffraction File (PDF) no. 6–464 [48]. Additionally, the XRD patterns of metallic Pt were not identified in any of the CuS-Pt/C films. This is likely due to the very low Pt loadings,

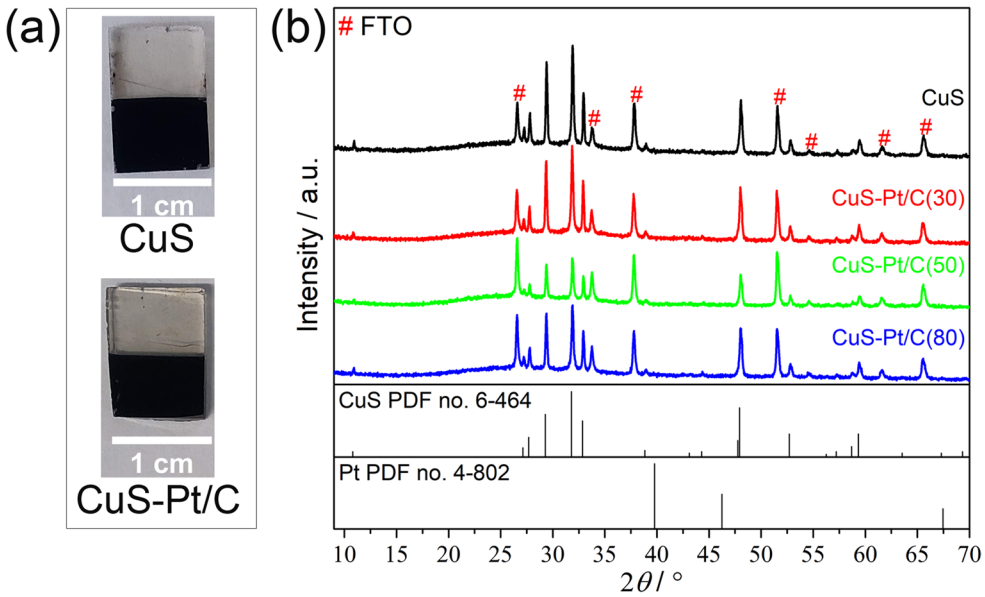

Fig. 3 **a** Photographs of bare CuS and CuS-Pt/C films. **b** XRD patterns of bare CuS and CuS-Pt/C films with different Pt loadings. Reference XRD patterns for CuS (PDF no. 6–464 [48]) and Pt (PDF no. 4–802 [49]) are also shown. The diffraction peaks of the FTO coating on the glass substrates are indicated by #

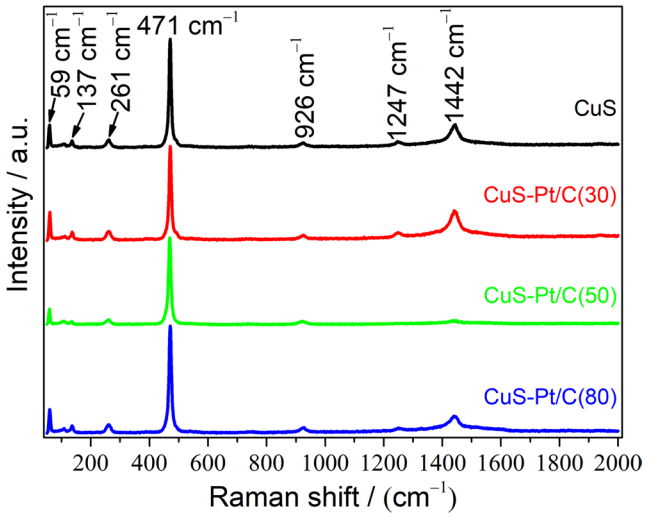

Fig. 4 Raman spectra of bare CuS and CuS-Pt/C films with different Pt loadings

as the estimated values were in the range of approximately 0.0036 to 0.0096 mg Pt cm^{-2}, obtained for the Pt/C load of 30 and 80 wt% Pt, respectively.

Additional physical characterisation of the films was performed via Raman spectroscopy, and the corresponding spectra are displayed in Fig. 4. The Raman spectra of both bare CuS and CuS-Pt/C films featured an intense band centred at 471 cm^{-1} corresponding to the A_{1g} longitudinal optical (LO) mode, which might arise due to the stretching vibration of S-S ions at the 4e sites [50, 51]. The spectra also displayed bands of low intensity at 59 and 137 cm^{-1} ascribed to the bending and lattice vibration modes of CuS [52]. A low-intensity band at 261 cm^{-1} is associated with the A_{1g} transverse optical mode, which is ascribed to the lattice vibration [50], and the band centred at 926 cm^{-1} is most likely to be linked with the 2LO mode of the second-order Raman spectra of CuS [53]. The Raman spectra for all samples also displayed low-intensity bands at 1247 and 1442 cm^{-1}, which, to the best of our knowledge, have not been assigned yet. Since such bands cannot be associated to secondary phases, namely, CuO (the most intense band at ca. 298 cm^{-1} [54]), Cu_2O (the most intense band at ca. 220 cm^{-1} [55]), elemental sulphur (the most intense band at 220 cm^{-1} for orthorhombic S_8 [56]), and copper sulphate (main band at ca. 970 cm^{-1} [53]), we believe they are related to second-order Raman scattering processes in CuS. The phenomenon of second-order Raman scattering has been observed in binary copper-based compounds (i.e., CuO [57] and CuI [58]), which could imply, despite differences between these materials and CuS, a possible trend of second-order Raman scattering phenomenon in binary copper-based materials. Additional studies would be needed to better assign these bands. In addition to this observation, it is worth highlighting that the presence of all the other bands in the Raman spectra confirms the formation of the CuS phase, which is in accordance with the findings of XRD results (cf. Figure 3b). Still regarding Fig. 4, the Raman spectra of CuS-Pt/C films did not display the characteristic bands of carbon, namely, the D and G bands centred at ca. 1320 and 1580 cm^{-1} [59], respectively. The absence of these carbon-related bands might be linked to the small amount of Pt/C materials deposited as mentioned above.

The bare CuS and CuS-Pt/C films were also characterised in terms of their optical properties, and that entailed estimating the films' optical E_g (for an allowed indirect electronic transition) by means of the Tauc plots (cf. Figure 5a). The estimation of the optical E_g was performed according to the protocol reported by Chen et al. [43], which consisted of drawing a line tangent to the baseline (dashed line) and another one tangent to the slope in the linear region (solid line) of the Tauc plot, and the E_g value was obtained from the intersection of these two lines (see Fig. 5a). The optical E_g value for the bare CuS film was ca. 1.59 eV (cf. Figure 5b), which is in accordance with other studies (1.44–1.55 eV) [60, 61]. For the CuS-Pt/C films with different Pt loadings, the optical E_g value of these films does not show an obvious change compared to that of the bare CuS film (cf. Figure 5b), suggesting that the optical properties of the CuS films are not significantly altered upon their superficial modification with the Pt/C materials.

The morphology of the films was analysed by scanning electron microscopy (SEM), as shown in Fig. 6. The SEM

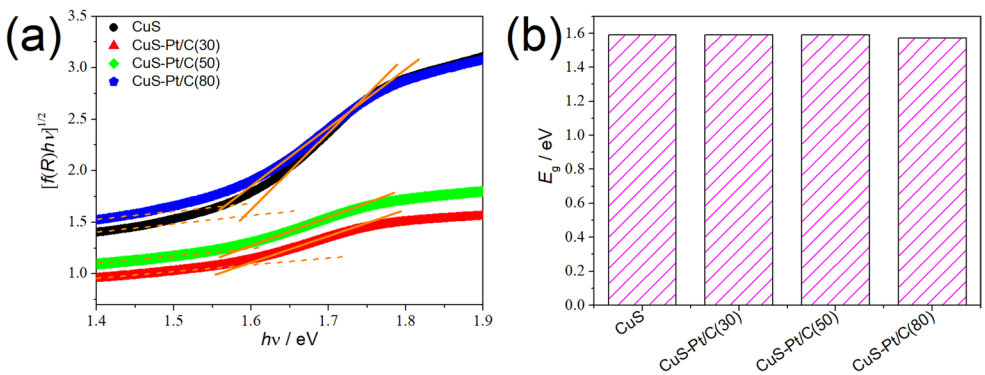

Fig. 5 **a** Tauc plots and **b** allowed indirect E_g values of bare CuS and CuS-Pt/C films with different Pt loadings

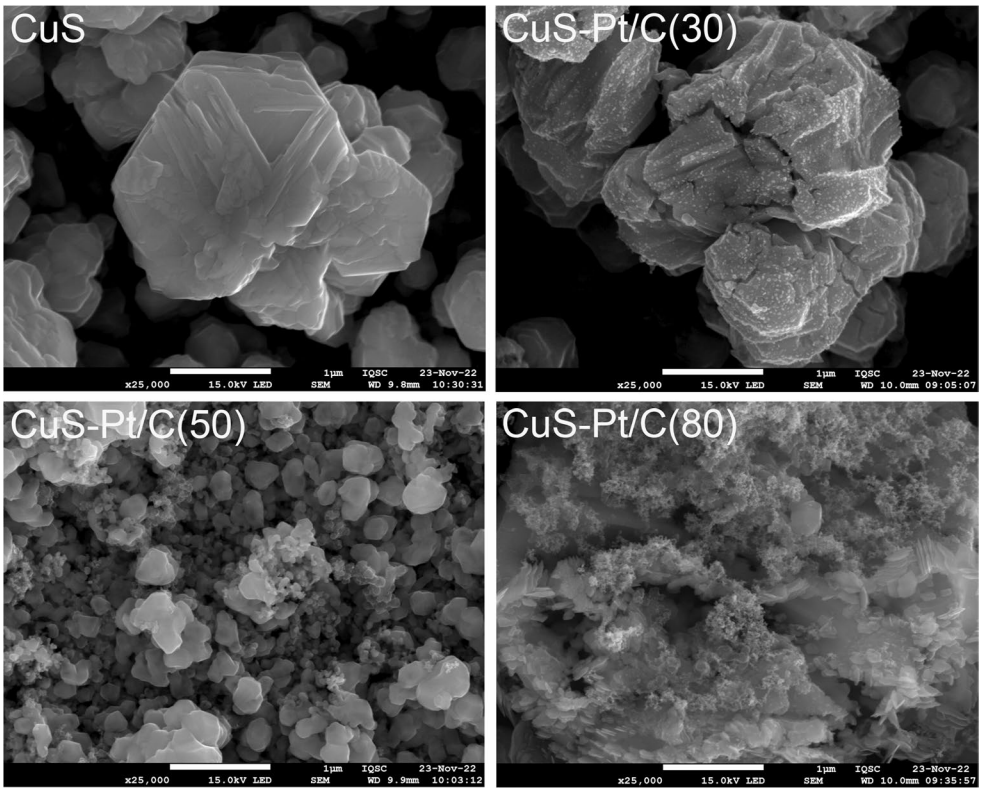

Fig. 6 SEM micrographs with a magnification of 25,000 times for bare CuS and CuS-Pt/C films with different Pt loadings

micrograph of the bare CuS film shows only large structures of irregular size and shape, which were greatly modified superficially after printing the Pt/C materials. Small clusters/particles were observed for the printed layer Pt/C(30), whereas for the CuS-Pt/C(50) and CuS-Pt/C(80) films, densely and highly dispersed packed particle aggregates of Pt/C seem to be present on top of the CuS film. In summary, based on these results, it can be inferred that the surface of the CuS films was effectively modified by the inkjet-printed Pt/C materials.

The chemical composition evaluation of the samples was performed by means of energy-dispersive X-ray spectroscopy (EDS). The EDS elemental mappings of all the CuS-containing films (cf. Figure 7) evidence the presence of the Cu and S elements. In the case of the bare CuS film, the Cu/S atomic ratio obtained from the EDS spectrum (Fig. S5a) was 0.995 (Table S1), which is very close to the ideal stoichiometry (i.e., Cu/S = 1). For the CuS-Pt/C films (see Fig. 7), the results show that the CuS-Pt/C(30) film displayed a uniform distribution of the Pt and C elements over the CuS film, whereas agglomerations of Pt and C are possibly present for the CuS-Pt/C(50) and CuS-Pt/C(80) films. Concerning the atomic percentage value of Pt, it was observed to be 6.0 at% Pt for the CuS-Pt/C(80) film, and 0.05 and 0.10 at% Pt for the CuS-Pt/C(30) and CuS-Pt/C(50) films, respectively (cf. Figure S5b and Table S1).

Additionally, chemical characterisation of the CuS-Pt/C films was carried out by X-ray photoelectron spectroscopy (XPS). We performed this analysis only for the CuS-Pt/C(50) film, as it exhibited the highest PEC performance for the HER (Fig. 9b). As shown in Fig. 8a, the high-resolution XPS spectrum of the Cu 2p core level of the CuS-Pt/C(50) film displays two doublets. The first doublet, with photoemission peaks at 932.4 eV (Cu $2p_{3/2}$) and 952.1 eV (Cu $2p_{1/2}$), is ascribed to Cu^{+} in the CuS [62], whereas the second doublet, having photoemission peaks at 933.6 eV (Cu $2p_{3/2}$) and 953.3 eV (Cu $2p_{1/2}$), is attributed to Cu^{2+} in CuS [62]. It is also noted a low-intensity and broad shake-up satellite peak (Fig. 8a), which arises from the presence of Cu^{2+} species [62]. The high-resolution XPS spectrum of the S 2p core level (cf. Figure 8b) of the CuS-Pt/C(50) film shows a doublet with photoemission peaks at 167.5 eV (S $2p_{3/2}$) and 168.7 eV (S $2p_{1/2}$) assigned to the SO_x species, which may have arisen due to the film's surface oxidation during air exposure [63]. Also, for the S 2p core level spectrum (Fig. 8b), the presence of another two doublets is seen, the first one at 161.9 eV (S $2p_{3/2}$) and 163.0 eV (S $2p_{1/2}$), attributed to the S^{2-} in CuS [62], and the second one presenting peaks at 163.6 eV (S $2p_{3/2}$) and 164.8 eV (S $2p_{1/2}$), associated with S_2^{2-} in CuS [62]. All these results indicate that a fraction of Cu in the CuS can be with an oxidation state of + 2 and another fraction as + 1 oxidation state, and S is present as S^{2-} and S_2^{2-}; therefore, CuS can be better formulated as $Cu^{I}_2Cu^{II}(S_2)S$, as reported in previous studies [62, 64].

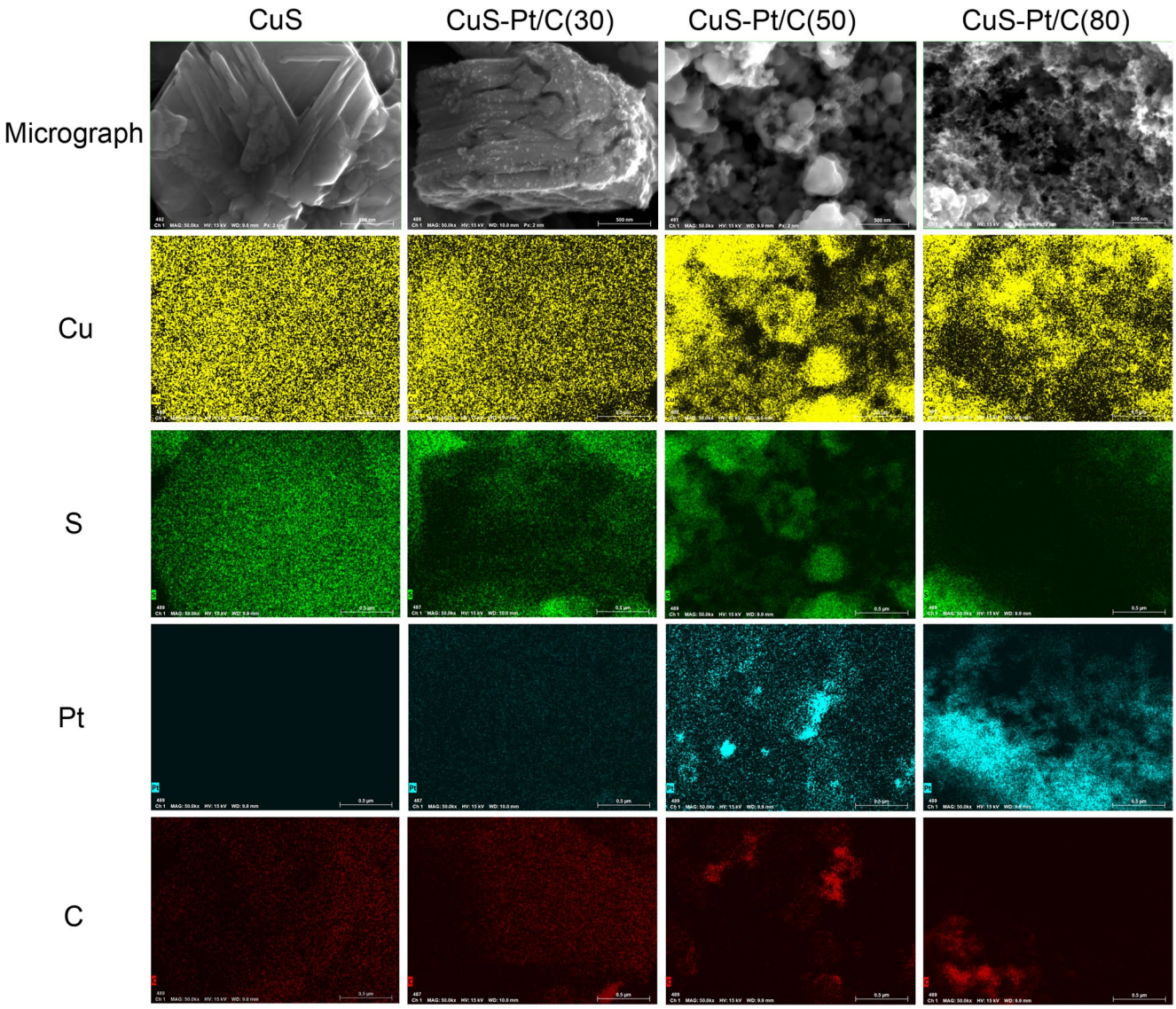

Fig. 7 EDS elemental mapping of Cu, S, Pt, and C of bare CuS and CuS-Pt/C films with different Pt loadings

In the case of the Pt 4f core level high-resolution XPS spectrum, an initial remark is that there is a significant overlap of the Pt 4f and Cu 3p regions [65, 66], which makes it difficult to distinguish between Pt and Cu elements. Although the profile of the high-resolution spectrum of the Pt 4f + Cu 3p core levels in Fig. 8c suggests, at first glance, predominance of Cu 3p signal [65, 66] and very low photoemission signal from Pt 4f, deconvolution of the spectrum is necessary to further verify this hypothesis. However, we find it challenging to deconvolute the Pt 4f + Cu 3p spectra of the CuS-Pt/C(50) film containing ultra-low Pt loading. Therefore, to avoid misinterpreting the Pt 4f + Cu 3p spectrum, a peak model was not constructed to fit the XPS spectrum in Fig. 8c. Despite this, the presence of Pt in the CuS-Pt/C films was confirmed by the EDS spectra (Fig. S5a) and elemental mapping (Fig. 7), which show that Pt presence is more noticeable in the sample with the highest Pt loading, namely, CuS-Pt/C(80) film. Regarding the high-resolution XPS spectrum of the C 1 s core level (cf. Figure 8d), the spectrum displayed peaks at 284.7, 285.5 and 288.3 eV, which are associated with the presence of C-C, C-O, and O-C=O [67], respectively, in the carbon black (Vulcan XC-72) used as a support for the Pt co-catalyst.

The PEC H_2 generation on the CuS and CuS-Pt/C films was investigated by LSVs run in the dark and under illumination from a solar simulator (irradiance of 100 mW cm^{-2}). It is worth mentioning that the photoelectrochemical decomposition process of CuS did not occur significantly during the PEC experiments, as the LSV measurements of each sample took less than 1 min. As shown in Fig. 11b (discussed later), the films remain satisfactorily stable for 20 min during the PEC experiment. Regarding the LSVs in Fig.

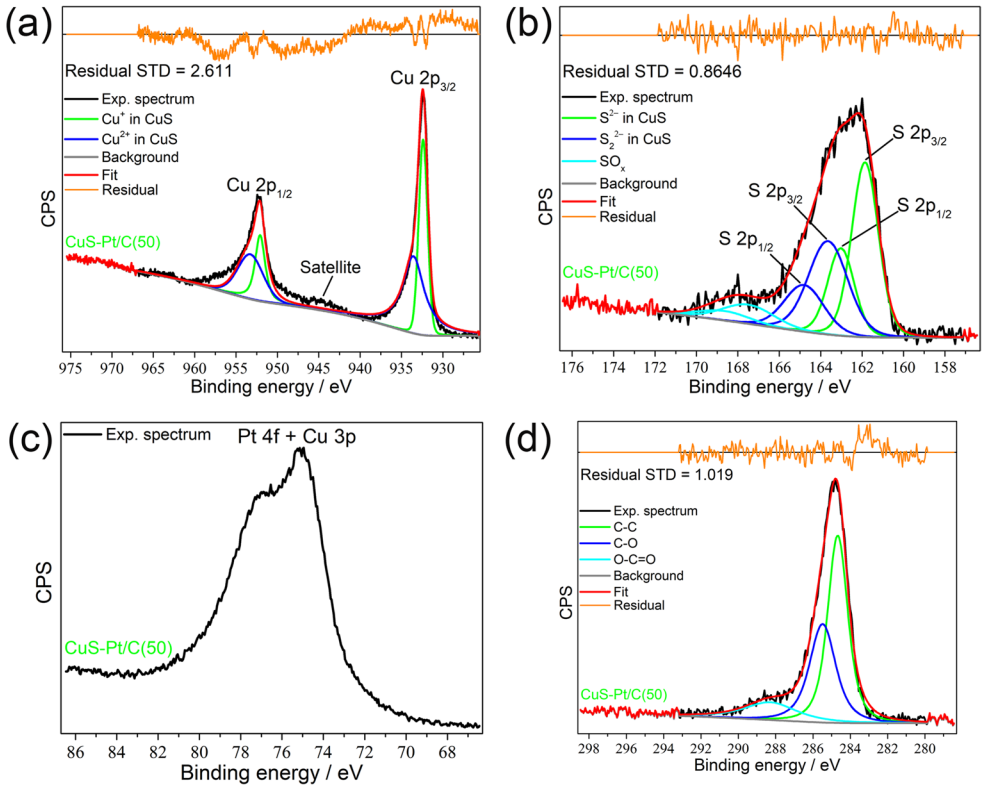

Fig. 8 High-resolution XPS spectra of **a** Cu 2p, **b** S 2p, **c** Pt 4f+Cu 3p, and **d** C 1 s core levels of CuS-Pt/C (50) film. Residual standard deviation plots are also displayed along with the corresponding XPS spectra

9a, it is noted that both CuS and CuS-Pt/C films displayed cathodic photocurrent density, which is ascribed to the light-driven HER. The occurrence of this process is thermodynamically feasible owing to the E_{cb} of CuS having a value more negative compared to that of the potential of the HER [24], which permits the transfer of the photogenerated electrons from the conduction band of CuS to reduce H_3O^+ species to generate H_2. Moreover, the occurrence of a cathodic current density signal under illumination suggests that the CuS films are p-type semiconductor materials, which is in accordance with the other studies [61]. Concerning the cathodic photocurrent density values (obtained from the difference of current density in the presence and absence of illumination) for the HER, the bare CuS film delivered a value of (−0.40 ± 0.09) mA cm^{-2} at 0 V vs. RHE (see Fig. 9b). The presence of the inkjet-printed Pt/C materials enabled a notable improvement of photoelectroactivity for the HER, as shown by the cathodic photocurrent density for the CuS-Pt/C(30), CuS-Pt/C(50) and CuS-Pt/C(80) films that featured values of (−3.17 ± 0.56), (−2.97 ± 0.54) and (−1.66 ± 0.38) mA cm^{-2} at 0 V vs. RHE, respectively. The increase of activity was 7.93- and 7.43-fold for the CuS-Pt/C(30) and CuS-Pt/C(50) films, respectively, in comparison with the bare CuS film. The improved photoelectroresponse of the CuS-Pt/C(30) and CuS-Pt/C(50) films is surely linked to the increased atomic percentage of Pt species in the inkjet-printed Pt/C materials (Table S1). However, as shown in Fig. 9b, the CuS-Pt/C(80) films featuring the highest nominal Pt loading (i.e., 80 wt% Pt in Pt/C) presented a decreased activity compared to (30 wt% and 50 wt%), albeit the photoelectroresponse of the CuS-Pt/C(80) film is still 4.15-fold higher than that of the bare CuS film. Besides the increase of the cathodic photocurrent density value, the onset potential (E_{on}) under illumination, estimated via the tangent method [68] (see Fig. S6), featured positive values for the CuS-Pt/C films (up to approximately 0.025 V vs. RHE) relative to that of the bare CuS film (E_{on} of ca. −0.013 V vs. RHE), as shown in Fig. 9c. These E_{on} values for the HER, featuring positive shifts under illumination, indicate a co-catalytic contribution of the Pt in the Pt/C materials present on the surface of the CuS films. This co-catalytic attribution, based on the positive shift of the E_{on}, aligns with studies in the literature [69, 70]. The co-catalytic effect can occur because Pt has active sites [71] that enhance H_2 generation kinetics; therefore, the improved PEC activity of the CuS-Pt/C films is due to the presence of Pt, which catalyses the HER. Regarding the contribution of the employed carbon black material (i.e., Vulcan XC-72) in the Pt/C system, although pristine carbon black possesses negligible electrocatalytic activity for the HER compared to metal catalysts [72], this material also plays an important role in enhancing the PEC performance of the CuS-Pt/C films. Carbon has a suitable work function (ϕ) value (−4.94 eV vs. vacuum level [73]), which allows this material to collect the photogenerated electrons from the CuS and then transfer them to Pt so to promote the HER (Fig. 10b). Furthermore, the good electrical conductivity of

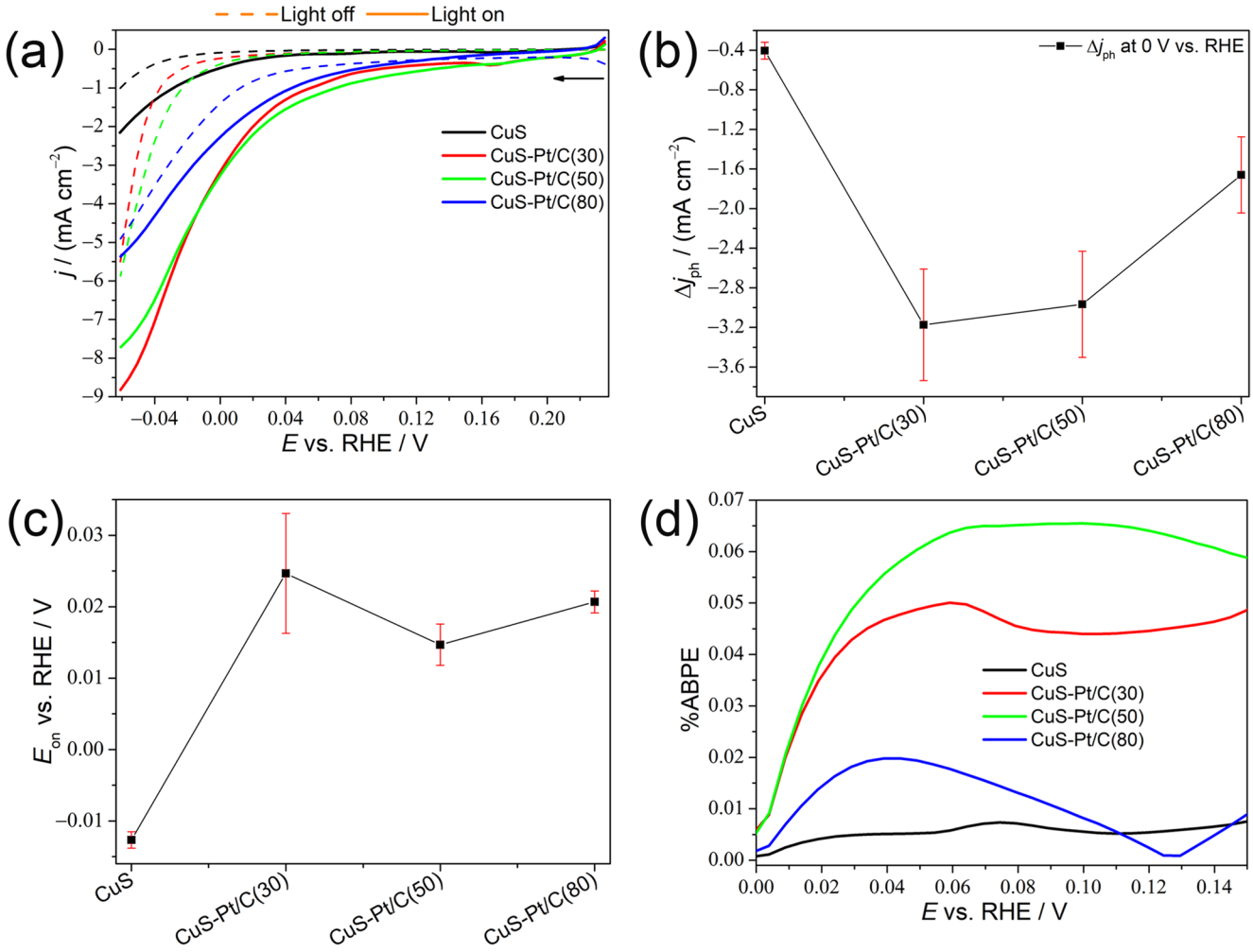

Fig. 9 **a** Linear sweep voltammograms at a scan rate of 50 mV s^{-1} in the dark and under solar simulator (irradiance of 100 mW cm^{-2}), **b** average cathodic photocurrent density (Δj_{ph}) values at 0 V vs. RHE, **c** estimated E_{on} values under illumination, and **d** ABPE plots of bare CuS and CuS-Pt/C films with different Pt loadings. The electrolyte was a N_2-saturated solution of 1.0 mol L^{-1} H_2SO_4 at a pH of 0.72 (as measured)

carbon black [74] may have also contributed to the transport of the photogenerated electrons and thereby enhanced the PEC performance of the photoelectrodes. Another key role of carbon black is as a catalyst support due to its high-surface area, which enables the fine dispersion of metal catalyst particles over the porous carbon structure, resulting in greater exposure of catalytically active atoms [72, 75]. Overall, carbon black contributed to the improvement of the PEC performance of the CuS-Pt/C films via two factors: (i) good electrical conductivity and (ii) a large surface area, which can anchor a larger number of Pt nanoparticles.

The PEC performance of the CuS and the CuS-Pt/C films for the HER was also assessed via the applied bias photon-to-current efficiency (ABPE), which was calculated from Eq. 4 [43] and employing the LSVs data (Fig. 9a). It should be highlighted that the ABPE data was achieved for a three-electrode cell set-up (i.e., bias was applied between the WE and RE), meaning that this efficiency represents only the PEC performance efficiency at the photocathode|electrolyte interface and does not stand as the efficiency of an entire PEC device. Nevertheless, ABPE can provide useful insights to better comprehend the PEC performance of a photoelectrode.

$$\mathrm{ABPE} = \frac{\left|\Delta j_{\mathrm{ph}}\right| \left(\left|E\,(\mathrm{vs.\ RHE})\right| - 0\right) \eta_{\mathrm{F}}}{P_{\mathrm{total}}}, \tag{4}$$

where E(vs. RHE) is the applied potential relative to the RHE, Δj_{ph} is the cathodic photocurrent density at a given E(vs. RHE) value, η_F is the Faradaic efficiency for the HER (it was considered 100% efficiency), and P_{total} is the solar simulator irradiance on the photoelectrodes (100 mW cm^{-2}).

According to Fig. 9d, the maximum ABPE for the CuS, CuS-Pt/C(30), CuS-Pt/C(50), and CuS-Pt/C(80) films was

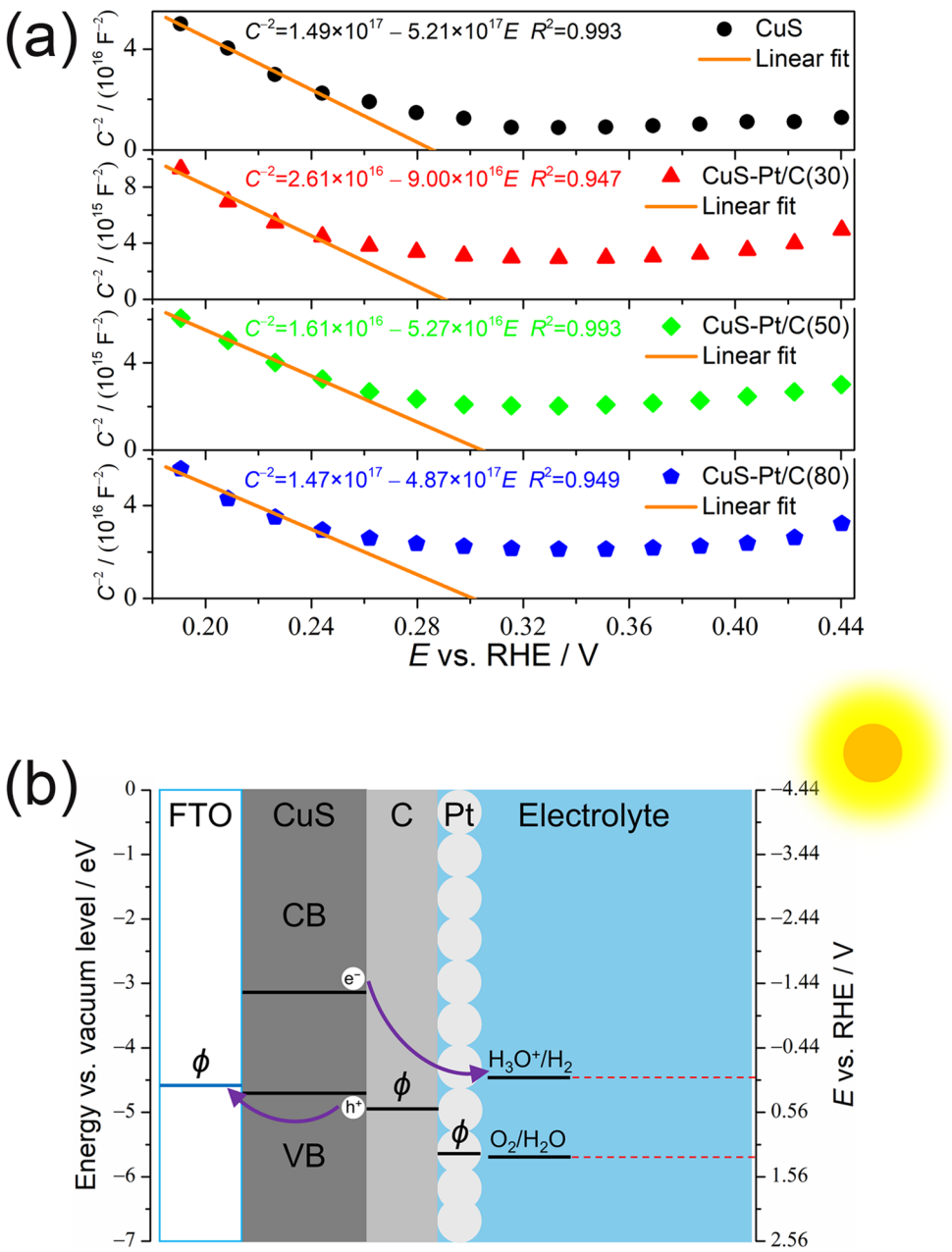

Fig. 10 **a** Mott-Schottky plots of bare CuS and CuS-Pt/C films with different Pt loadings. The electrolyte was a N_2-saturated solution of 1.0 mol L^{-1} H_2SO_4 at a pH of 0.72 (as measured). **b** Band diagrams of FTO/CuS/Pt/H_2O with positions relative to the energy vs. vacuum level and potential vs. RHE. The valence band (VB) and CB edge positions of CuS were calculated from Eqs. S1-S4. Since the ϕ of FTO varies from 4.48 to 4.73 eV (after solvent cleaning) [77], an average value was taken. The ϕ of C and polycrystalline Pt were taken from Jiang et al. [73] and Michaelson [78], respectively

approximately 0.0058%, 0.050%, 0.064% and 0.018% at 0.059 V vs. RHE, respectively. These results evidence that, compared to that of the bare CuS film, the highest increments were 8.62- and 11.0-fold for the CuS-Pt/C(30) and the CuS-Pt/C(50) films, respectively. This suggests that the presence of these Pt/C loadings provided a considerable improvement in PEC efficiency at the CuS-Pt/C|electrolyte interface for the HER at positive potential values.

We also recorded Mott-Schottky curves for the bare CuS film and the CuS-Pt/C films. As displayed in Fig. 10a, the linear portion of the Mott-Schottky plots appearing at low overpotentials featured a negative slope for all the samples, which is characteristic of semiconductor materials with p-type conductivity. The Mott-Schottky data were also employed to estimate the E_{fb} (see Eq. 5) [43], which is defined as the potential at which there is no excess of charge at the semiconductor|electrolyte interface, namely, the electric field is zero and there is no space charge region at the semiconductor|electrolyte interface (the bands are not bent) [45]. E_{fb} is an important parameter for the construction of the band structure of a semiconductor, and knowing the band structure is crucial to observing whether a semiconductor material can promote water splitting under illumination [43].

$$E_{fb}\,(\text{vs. RHE}) + \frac{kT}{e} = \text{x-intercept} = -\frac{\text{linear coefficient}}{\text{angular coeficiente}}, \quad (5)$$

where k is the Boltzmann constant (1.38×10^{-23} J K^{-1}), T is the temperature (298.15 K), e is the elementary charge (1.60×10^{-19} C), and the linear and angular coefficient values are those given by the linear equations of the lines in Fig. 10a.

The estimated E_{fb} value of the bare CuS film is 0.26 V vs. RHE, whereas for the CuS-Pt/C(30), CuS-Pt/C(50) and CuS-Pt/C(80) films are 0.26, 0.28, and 0.28 V vs. RHE, respectively. According to these results, the maximum shift of the E_{fb} relative to the CuS film is 20 mV vs. RHE towards more positive potentials for the CuS-Pt/C(50 and 80) films. Since the value of E_{fb} of a p-type semiconductor is expected to be close to the valence band edge potential (E_{vb}) [76], the slight shift of the E_{fb} (7.7% increase) towards more positive values suggests that the E_{vb} of the CuS-Pt/C films is slightly more positive, compared to the bare CuS film. Additionally, the Mott-Schottky data (Fig. 10a) and E_g values (Fig. 5b) were employed to construct the band diagram of the CuS film; calculation details are provided in the Supplementary Information. As shown in Fig. 10b, the position of the conduction band (CB) edge of CuS, and the ϕ of the C and Pt are suitably aligned for the transport of the photogenerated electrons towards the surface of the photoelectrode to drive the HER.

The PEC stability of the CuS-Pt/C films was evaluated by the H_2 measurement, in which the gas was collected from the headspace of the cell at different times over 3 h of running the PEC experiment with the CuS-Pt/C film under illumination and polarised at −0.04 V vs. RHE. This experiment was performed only for the CuS-Pt/C(30) film, as it provided the highest average cathodic photocurrent density response (see Fig. 9b). For the bare CuS film, similar measurements were performed; however, the amount of H_2 generated was below the quantification limit of the equipment. As shown in Fig. 11a, the maximum PEC H_2 generation of CuS-Pt/C(30) film was 144.8 µmol at −0.04 V vs. RHE (corresponding to a Faradaic efficiency of 69.8%) during 30 min of PEC experiment, and beyond this time, the amount of generated H_2 considerably decreased, reaching a condition of no H_2 production for times longer than 90 min. A similar trend was observed for the cathodic photocurrent density of CuS-Pt/C(30) film at −0.04 V vs. RHE that displays no significant decay up to 20 min of PEC experiment, which is the stability time, and for times longer than this the cathodic photocurrent density considerably diminishes until a point where there is no photocurrent density (see Fig. 11b). This decay of the amount of H_2 generated and the cathodic photocurrent density, as well as the Faradaic efficiency for the HER being lower than the expected 100%, indicate the occurrence of photoelectrochemical decomposition of CuS film. This process is thermodynamically favourable due to the potential for cathodic decomposition by electrons of CuS being less negative than its E_{cb} (see Fig. S7), meaning that CuS can undergo self-photoreduction by its photogenerated electrons. Calculation of decomposition potential for CuS was performed following the approach developed by Gerischer [79, 80], and the calculation details are found in the Supplementary Information.

Additional understanding of the photoelectrochemical decomposition of the CuS-Pt/C films was achieved via physical and chemical characterisation after the PEC stability experiments. The stability experiments consisted of polarising the photoelectrode at −0.24 V vs. $Ag/AgCl/Cl^-_{(sat.\ KCl)}$ (0 V vs. RHE) for 1 h under a solar simulator (irradiance at the photoelectrodes was 478 mW cm^{-2}). The CuS-Pt/C(80) film was chosen for this PEC stability experiment, as it has the highest Pt loading, which facilitates its identification by the characterisation techniques (SEM and EDS). According to the SEM micrographs, the morphology of the CuS-Pt/C film did not undergo obvious modifications after the PEC stability experiments (Fig. S8). However, the chemical composition of the CuS-Pt/C film was considerably affected by the PEC stability experiment. The Cu/S atomic ratio of the CuS-Pt/C film, obtained from the EDS spectrum (Fig. S9), was 2.6 times higher after the PEC experiment (Table S4), indicating that sulphur-based species are removed from the photoelectrodes, which supports our hypothesis about the photoelectrochemical decomposition of the CuS films (Fig. S7). The CuS-Pt/C film also showed an increase in the C/Pt atomic ratio (2.7 times higher) after the PEC stability experiment (Table S4), indicating that Pt content is lower due to its detachment from the CuS-Pt/C film during the

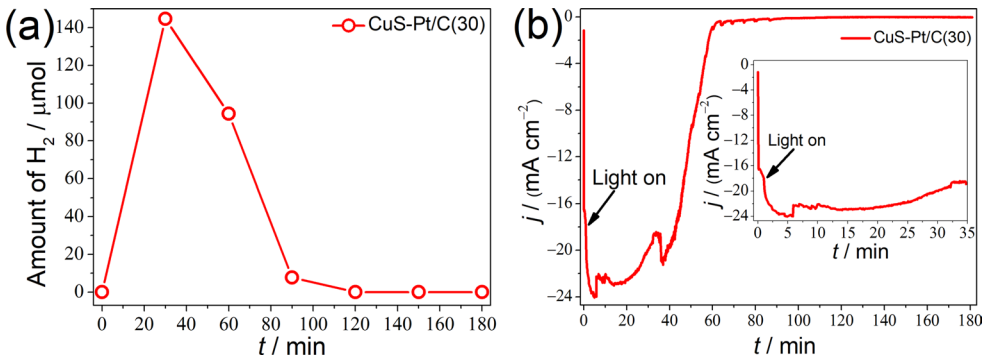

Fig. 11 **a** Plot of the amount of H_2 generated and its corresponding **b** chronoamperogram of CuS-Pt/C(30) film polarised at −0.04 V vs. RHE and under solar simulator (the irradiance on the film's surface corresponded to approximately 3 suns). The electrolyte was a N_2-saturated solution of 1.0 mol L^{-1} H_2SO_4 at a pH of 0.72 (as measured)

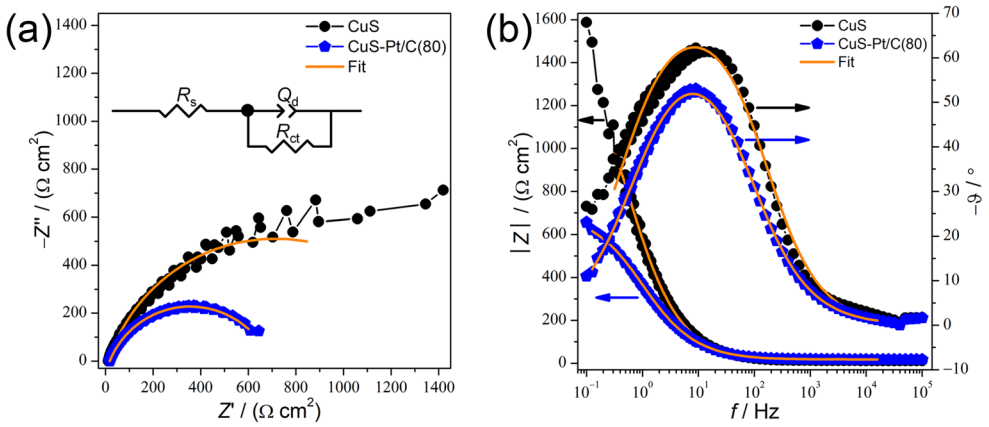

Fig. 12 **a** Complex-plane impedance diagrams and their corresponding **b** Bode diagrams at 0 V vs. RHE and under solar simulator (irradiance of 100 mW cm^{-2}) of bare CuS and CuS-Pt/C(80) films. The electrolyte was a N_2-saturated solution of 1.0 mol L^{-1} H_2SO_4 at a pH of 0.72 (as measured). The inset of Fig. 12a displays the equivalent electric circuit model employed to fit the EIS spectra

stability test. The detachment process of Pt during PEC stability experiments has also been demonstrated in literature studies for other photoelectrodes [81]. XPS measurements were also performed on the CuS-Pt/C(30) film after the PEC stability experiment (run for 1 h under solar simulator irradiance of 478 mW cm^{-2} and the film polarised at 0 V vs. RHE). As shown in Fig. S10a, the high-resolution XPS spectrum of the Cu 2p core level displays obvious change after PEC stability; for instance, one notices shoulder peaks at 934.3 eV (Cu $2p_{3/2}$) and 954.0 eV (Cu $2p_{1/2}$) assigned to Cu^{2+} in $Cu(OH)_2$ [82, 83], and the presence of noticeable shake-up satellite peaks, which are indication of $Cu(OH)_2$ presence [82, 83]. Moreover, another doublet is observed at 932.5 eV (Cu $2p_{3/2}$) and 952.3 eV (Cu $2p_{1/2}$), which is associated with the Cu^+ and/or metallic Cu [82, 83]. According to these results, the photoelectrochemical decomposition of the CuS-Pt/C film may have led to the formation of $Cu(OH)_2$, as well as Cu^+ species and/or metallic Cu during the PEC stability experiment. Regarding the high-resolution XPS spectra of the S 2p, Pt 4f + Cu 3p, and C 1s core levels (Figs. S10b-d), no obvious change was noted in the profile of these spectra after PEC stability.

Seeking to learn more about the role of Pt/C on the PEC improvement of the CuS-Pt/C films, we recorded impedance spectra of the bare CuS and CuS-Pt/C(80) films under illumination (irradiance of 100 mW cm^{-2}) and polarised at 0 V vs. RHE. It is important to highlight that the photoelectrochemical decomposition of CuS was not significant during the impedance measurements, as this process is more prominent at −0.04 V vs. RHE after 20 min of PEC experiment (see discussion of Fig. 11), and the impedance experiments were performed at 0 V vs. RHE. The complex-impedance diagrams of all the films apparently display one semicircle (Fig. 12a), and the Bode diagrams also evidence only one phase angle (ϑ) peak (plot of $-\vartheta$ vs. f, Fig. 12b), which, at first glance, suggest occurrence of only one charge transfer process. Based on these observations and aiming to better understand the charge transfer process(es), we fitted

Table 1 Resistance and capacitance density values obtained from the equivalent electric circuit model used to fit the EIS spectra

Sample	R_{ct} (Ω cm^2)	Q_d (S cm^{-2} s^{α})	α_f	C_d(F cm^{-2})
CuS	1405	3.20×10^{-4}	0.80	2.62×10^{-4}
CuS-Pt/C(80)	676.7	4.83×10^{-4}	0.75	3.33×10^{-4}

the impedance spectra with an equivalent electric circuit model comprised of a solution resistance (R_s) connected in series with a RQ component (R is the resistance and Q is the constant phase element (CPE)), as shown in the inset of Fig. 12a. The R was assigned to the charge transfer resistance (R_{ct}) at the photocathode|electrolyte interface, and the Q is associated with the double-layer pseudocapacitance density (Q_d) of the photocathodes. The Q was employed to better model the double-layer capacitance density (C_d) of the photoelectrodes, and the actual value of the C_d was obtained from Eq. 6 [84].

$$C_d = \frac{(Q_d R_{ct})^{\frac{1}{\alpha_f}}}{R_{ct}}, \tag{6}$$

where Q_d is the pseudocapacitance density, also known as CPE-T, and α_f is the CPE exponent, also known as CPE-P. The α_f features value from 0 to 1, and $\alpha_f = 1$ is for a Q that acts as an ideal capacitor.

The fitting results and their corresponding error percentages for all the samples are listed in Tables 1 and S5, respectively. According to Table 1, the R_{ct} value of the CuS-Pt/C(80) film decreased by 2.1 times compared to that of the bare CuS film, which indicates improved transfer of the photogenerated charge carriers of the CuS-Pt/C film for the occurrence of the HER. Moreover, the Bode plots (Fig. 12b) show at lower frequency a considerable decrease in the impedance magnitude ($|Z|$) of about 2.4 times upon the presence of Pt/C materials, whereas at higher frequencies no obvious change of $|Z|$ was observed for the CuS-Pt/C(80) film compared to that of the CuS film. It is important to note that the high- and low-frequency domains of the Bode plots correspond to the charge transfer process in the

semiconductor's bulk and at the semiconductor|electrolyte interface, respectively [85, 86]. This means that the diminished $|Z|$ values at lower frequencies points out that the presence of Pt/C on the surface of the CuS films facilitates the transfer of the photogenerated electrons at the CuS-Pt/C|electrolyte interface for the occurrence of the HER, which explain the enhanced cathodic photocurrent density values (see Fig. 9b). The facilitation of the transfer of the photogenerated electrons may have also hindered the electron-hole recombination process, as evidenced in another study [30].

Regarding the C_d values displayed in Table 1, there was a percentage increment of ca. 27% for the CuS-Pt/C(80) film compared to that of the bare CuS film. This increase in the C_d is probably due to the enlargement of the electrochemically active surface area (ECSA) of the CuS-Pt/C films in comparison to the bare CuS film. Furthermore, according to the SEM micrographs (cf. Figure 6), the surface of the CuS-Pt/C(80) film is apparently rougher than that of the bare CuS film, which backs up our hypothesis about the increase of ECSA. The probable increased surface area of the CuS-Pt/C(80) film may have also contributed to the improvement of PEC activity (see Fig. 9) as a larger surface area leads to exposure of a higher number of active sites for taking place the light-driven HER.

Conclusions

In summary, we successfully modified the surface of the CuS films by inkjet printing Pt/C material with ultra-low Pt loading for improving the HER under illumination. The presence of the Pt/C material over the CuS films provided a substantially high photocurrent density response for the HER of −3.17 mA cm^{-2} at 0 V vs. RHE, corresponding to a 7.93-fold increase compared to that of the bare CuS film. This improved PEC performance for H_2 generation via water splitting was ascribed to the facilitation of photogenerated electrons transfer at the CuS-Pt/C|electrolyte interface, as noted by the decrease of the R_{ct} (2.1-fold) of the impedance spectra. The improved PEC performance of the CuS-Pt/C films may also be linked to their enlarged ECSA relative to the bare CuS film, as evidenced by the higher values of C_d (ca. 27% higher) obtained from the impedance spectra. The presence of the inkjet-printed Pt/C materials over CuS film also resulted in positive E_{on} values under illumination (up to approximately 0.025 V vs. RHE) compared to that of the bare CuS film (ca. −0.013 V vs. RHE), which implies that the HER was co-catalysed under illumination by the Pt in the Pt/C materials, thereby enhancing the PEC performance. Evaluation of the PEC stability of the CuS-Pt/C film shows a stable cathodic photocurrent density at −0.04 V vs. RHE during a 20 min PEC experiment. Longer times result in considerable decay of the cathodic photocurrent density due to photoelectrochemical decomposition of CuS. A similar behaviour of stability was observed for the amount of H_2 generated by the CuS-Pt/C film at −0.04 V vs. RHE under illumination. Overall, this work features, as a new contribution, the employment of a commercial low-cost inkjet printer to deposit Pt/C material with ultra-low Pt loading over CuS films to improve PEC activity for H_2 generation via solar-driven water splitting. Lastly, improvement of PEC performance in terms of stability under operational conditions, which is still a limiting factor, will be possible via additional surface modifications of CuS or CuS-Pt/C films.

Supplementary information The online version contains supplementary material available at https://doi.org/10.1007/s10008-026-06538-8.

Acknowledgements This study was financed, in part, by the São Paulo Research Foundation (FAPESP), Brazil. Process numbers #2021/01268-3 and #2019/22183-6. This study was financed in part by the Coordenação de Aperfeiçoamento de Pessoal de Nível Superior - Brasil (CAPES) - Finance Code 001. Additionally, we gratefully acknowledge the support of the RCGI – Research Centre for Greenhouse Gas Innovation (23.1.8493.1.9), hosted by the University of São Paulo (USP) and sponsored by FAPESP – São Paulo Research Foundation (#2020/15230-5) and Shell Brasil, as well as the strategic importance of the support given by ANP (Brazil's National Oil, Natural Gas and Biofuels Agency) through the R&DI levy regulation. We are grateful to Prof Dr Valmor R. Mastelaro from Universidade de São Paulo (USP), Brazil, for performing the XPS experiments on the samples. We also would like to acknowledge Dr Debora T. Balogh and Prof Dr Roberto M. Faria, both from Universidade de São Paulo (USP), Brazil, for permitting us to use the goniometer and viscometer.

Funding The Article Processing Charge (APC) for the publication of this research was funded by the Coordenação de Aperfeiçoamento de Pessoal de Nível Superior - Brasil (CAPES) (ROR identifier: 00x0ma614).

References

1. Anderson TR, Hawkins E, Jones PD (2016) CO_2, the greenhouse effect and global warming: from the pioneering work of

Arrhenius and Callendar to today's earth system models. Endeavour 40:178–187
2. Soued C, Harrison JA, Mercier-Blais S, Prairie YT (2022) Reservoir CO_2 and CH_4 emissions and their climate impact over the period 1900–2060. Nat Geosci 15(9):700–705
3. Canadell JG, Poulter B, Bastos A, Ciais P, Hayes DJ, Thompson RL, Villalobos Y (2022) In: Poulter B, Canadell JG, Hayes DJ, Thompson RL (eds) Balancing greenhouse gas budgets: accounting for natural and anthropogenic flows of CO_2 and other trace gases. Elsevier, Massachusetts
4. Ruhul M, Bhuiyan A (2022) Overcome the future environmental challenges through sustainable and renewable energy resources. Micro Nano Lett 17:402–416
5. Kumar A, Daw P, Milstein D (2022) Homogeneous catalysis for sustainable energy: hydrogen and methanol economies, fuels from biomass, and related topics. Chem Rev 122:385–441
6. Hosseini SE, Wahid MA (2016) Hydrogen production from renewable and sustainable energy resources: promising green energy carrier for clean development. Renew Sustain Energy Rev 57:850–866
7. Megía PJ, Vizcaíno AJ, Calles JA, Carrero A (2016) Hydrogen production technologies: from fossil fuels toward renewable sources. A mini review. Energy Fuels 35:16403–16415
8. Petrii O (2009) In: Garche J (ed) Encyclopedia of electrochemical power sources. Elsevier
9. Kumar SS, Lim H (2022) An overview of water electrolysis technologies for green hydrogen production. Energy Rep 8:13793–13813
10. Martínez NP, Isaacs M, Nanda KK (2020) Paired electrolysis for simultaneous generation of synthetic fuels and chemicals. New J Chem 44:5617–5637
11. Kim J, Yang M (2023) In: Scipioni A, Manzardo A, Ren J (eds) Hydrogen economy: supply chain, life cycle analisys and energy transition for sustainibility, 2nd edn. Elsevier
12. Zhang Y, Bu Y, Wang L, Ao J-P (2021) Regulation of the photogenerated carrier transfer process during photoelectrochemical water splitting: A review. Green Energy Environ 6:479–495
13. Guo M, Ma G (2020) Alteration of onset potentials of Rh-doped $SrTiO_3$ electrodes for photoelectrochemical water splitting. J Catal 391:241–246
14. Shi H, Guo H, Wang S, Zhang G, Hu Y, Jiang W, Liu G (2022) Visible light photoanode material for photoelectrochemical water splitting: A review of bismuth vanadate. Energy Fuels 36:11404–11427
15. Fushima A, Honda K (1972) Electrochemical photolysis of water at a semiconductor electrode. Nature 238:37–38
16. Reyes-Coronado D, Rodríguez-Gattorno G, Espinosa-Pesqueira ME, Cab C, de Coss R, Oskam G (2008) Phase-pure TiO_2 nanoparticles: anatase, brookite and rutile. Nanotechnology 19:145605
17. Costa MB, de Araújo MA, Tinoco MVdL, de Brito JF, Mascaro LH (2022) Current trending and beyond for solar-driven water splitting reaction on WO_3 photoanodes. J Energy Chem 73:88–113
18. Ros C, Andreu T, Morante JR (2020) Photoelectrochemical water splitting: a road from stable metal oxides to protected thin film solar cells. J Mater Chem A 8:10625–10669
19. Yang W, Zhang X, Tilley SD (2021) Emerging binary chalcogenide light absorbers: material specific promises and challenges. Chem Mater 33:3467–3489
20. Chandrasekaran S, Yao L, Deng L, Bowen C, Zhang Y, Chen S, Lin Z, Peng F, Zhang P (2019) Recent advances in metal sulfides: from controlled fabrication to electrocatalytic, photocatalytic and photoelectrochemical water splitting and beyond. Chem Soc Rev 48:4178–4280
21. Shaikh GY, Nilegave DS, Girawale SS, Kore KB, Newaskar SR, Sahu SA, Funde AM (2022) Structural, optical, photoelectrochemical, and electronic properties of the photocathode CuS and the efficient CuS/CdS heterojunction. ACS Omega 7:30233–30240
22. Isac L, Cazan C, Andronic L, Enesca A (2022) CuS-based nanostructures as catalysts for organic pollutants photodegradation. Catalysts 12:1135
23. Kalanur SS, Seo H (2017) Tuning plasmonic properties of CuS thin films via valence band filling. RSC Adv 7:11118–11122
24. Wojtyła S, Baran T (2019) Photocatalytic H_2 production over RuO_2@ZnS and RuO_2@CuS nanostructures. Int J Hydrogen Energy 44:14624–14634
25. Feng W, Nie W, Cheng Y, Zhou X, Chen L, Qiu K, Chen Z, Zhu M, He C (2015) In vitro and in vivo toxicity studies of copper sulfide nanoplates for potential photothermal applications, Nanomedicine Nanotechnology. Biol Med 11:901–912
26. Chen P, Zhang P, Cui Y, Fu X, Wang Y (2023) Recent progress in copper-based inorganic nanostructure photocatalysts: properties, synthesis and photocatalysis applications. Mater Today Sustain 21:100276
27. Vempuluru NR, Krishnan CK, Parnapalli R, Velusamy J, Marappan S, Pitchaimuthu S, Murikinati M, Venkatakrishnan SM (2021) Solar hydrogen generation from organic substance using Earth abundant CuS–NiO heterojunction semiconductor photocatalyst. Ceram Int 47:10206–10215
28. Guo H, Su C, Yu D, Li L, Liu Z, Han Z, Lu X (2019) Facile fabrication of ZnO/CuS heterostructure photoanode with highly PEC performance and excellent charge separation efficiency. J Electroanal Chem 854:113546
29. Du J, Yang M, Zhang F, Cheng X, Wu H, Qin H, Jian Q, Lin X, Li K, Kang DJ (2018) Enhanced charge separation of CuS and CdS quantum-dot-cosensitized porous TiO_2 -based photoanodes for photoelectrochemical water splitting. Ceram Int 44:3099–3106
30. Dubale AA, Tamirat AG, Chen H-M, Berhe TA, Pan C-J, Su W-N, Hwang B-J (2016) A highly stable CuS and CuS–Pt modified Cu_2O/CuO heterostructure as an efficient photocathode for the hydrogen evolution reaction. J Mater Chem A 4:2205–2216
31. Tinoco MVdL, Costa MB, Mascaro LH, de Brito JF (2021) Photoelectrodeposition of Pt nanoparticles on Sb_2Se_3 photocathodes for enhanced water splitting. Electrochim Acta 382:138290
32. Makagon E, Wachtel E, Merkle R, Lubomirsky I (2019) Solution deposition of Pt contacts suited to proton-conducting ceramics. Solid State Ionics 339:114994
33. Towne S, Viswanathan V, Holbery J, Rieke P (2007) Fabrication of polymer electrolyte membrane fuel cell MEAS utilizing inkjet print technology. J Power Sources 171:575–584
34. Deiner LJ, Reitz TL (2017) Inkjet and aerosol jet printing of electrochemical devices for energy conversion and storage. Adv Eng Mater 19:1600878
35. Breitwieser M, Klingele M, Britton B, Holdcroft S, Zengerle R, Thiele S (2015) Improved Pt-utilization efficiency of low Pt-loading PEM fuel cell electrodes using direct membrane deposition. Electrochem Commun 60:168–171
36. Bezerra CAG, Deiner LJ, Tremiliosi-Filho G (2020) Inkjet printed double-layered cathodes for PEM fuel cells. J Electrochem Soc 167:124503
37. Bezerra CAG, Deiner LJ, Tremiliosi-Filho G (2019) Unexpected performance of inkjet-printed membrane electrode assemblies for proton exchange membrane fuel cells. Adv Eng Mater 21:1900703
38. Taylor AD, Kim EY, Humes VP, Kizuka J, Thompson LT (2017) Inkjet printing of carbon supported platinum 3-D catalyst layers for use in fuel cells. J Power Sources 171:101–106

39. Strong A, Thornberry C, Beattie S, Chen R, Coles SR (2015) Depositing catalyst layers in polymer electrolyte membrane fuel cells: a review. J Fuel Cell Sci Technol 12:064001
40. de Araújo MA, Lucas FWS, Mascaro LH (2020) Effect of the electrodeposition potential on the photoelectroactivity of the SnS/Sb_2S_3 thin films. J Solid State Electrochem 24(2):389–399
41. Siegrist T (1997) Crystallographica - a software toolkit for crystallography. J Appl Cryst 30:418–419
42. Fairley N, Fernandez V, Richard-Plouet M, Guillot-Deudon C, Walton J, Smith E, Flahaut D, Greiner M, Biesinger M, Tougaard S, Morgan D, Baltrusaitis J (2021) Systematic and collaborative approach to problem solving using X-ray photoelectron spectroscopy. Appl Surf Sci Adv 5:100112
43. Chen Z, Dinh HN, Miller E (2013) Photoelectrochemical water splitting: Standards, experimental methods, and protocols. Springer
44. Harris-Lee TR, Marken F, Bentley CL, Zhang J, Johnson AL (2023) A chemist's guide to photoelectrode development for water splitting – the importance of molecular precursor design. EES Catal 1:832–873
45. Bard AJ, Faulkner LR, White HS (2022) Electrochemical methods: Fundamental and applications. Wiley, New York
46. Biswas TT, Yu J, Nierstrasz VA (2019) Efects of ink characteristics and piezo-electric inkjetting parameters on lysozyme activity. Sci Rep 9:18252
47. Xi F, Liu H, Li W, Zhu L, Geng H, Quan L, Liang W (2015) Fabricating CuS counter electrode for quantum dots-sensitized solar cells via electro-deposition and sulfurization of Cu_2O. Electrochim Acta 178:329–335
48. Kalbskopf R, Pertlik F, Zemann J (1975) Verfeinerung der Kristallstruktur des covellins, CuS, Mit Einkristalldaten. Tschermaks Mineral Und Petrogr Mitteilungen 22:242–249
49. Swanson HE, Tatge E (1953) Standard X-ray diffraction powder patterns - National Bureau of Standards Circular 539 Volume I
50. Marimuthu T, Anandhan N, Panneerselvam R, Ganesan KP, Roselin AA (2019) Synthesis and characterization of copper sulfide thin films for quantum dot sensitized solar cell and supercapacitor applications. Nano-Struct Nano-Objects 17:138–147
51. Ishii M, Shibata K, Nozaki H (1993) Anion distributions and phase transitions in $CuS_{1-x}Se_x$(x = 0–1) studied by Raman spectroscopy. J Solid State Chem 105:504–511
52. Yeryukov NA, Milekhin AG, Sveshnikova LL, Duda TA, Pokrovsky LD, Gutakovskii AK, Batsanov SA, Rodyakina EE, Latyshev AV, Zahn DRT (2014) Synthesis and characterization of Cu_xS (x = 1 − 2) nanocrystals formed by the Langmuir−Blodgett technique. J Phys Chem C 118:23409–23414
53. Smith GD, Clark RJH (2002) The role of H_2S in pigment blackening. J Cult Herit 3:101–105
54. Chrzanowski J, Irwin JC (1989) Raman scattering from cupric oxide. Solid State Commun 70:11–14
55. Balkanski M, Nusimovici MA, Reydellet J (1969) First order Raman spectrum of Cu_2O. Solid State Commun 7:815–818
56. Nims C, Cron B, Wetherington M, Macalady J, Cosmidis J (2019) Low frequency Raman spectroscopy for micron-scale and in vivo characterization of elemental sulfur in microbial samples. Sci Rep 9:7971
57. Litvinchuk AP, Möller A, Debbichi L, Krüger P, Iliev MN, Gospodinov MM (2013) Second-order Raman scattering in CuO. J Phys Condens Matter 25:105402
58. Hildebrandt R, Seifert M, George J, Blaurock S, Botti S, Krautscheid H, Grundmann M, Sturm C (2023) Determination of acoustic phonon anharmonicities via second-order Raman scattering in CuI. New J Phys 25:123022
59. Tyagi D, Varma S, Bharadwaj SR (2018) XPS and Raman studies of Pt catalysts supported on activated carbon. AIP Conf Proc 1942:140023
60. Nair MTS, Guerrero L, Nair PK (1998) Conversion of chemically deposited CuS thin films to $Cu_{1.8}S$ and $Cu_{1.96}S$ by annealing. Semicond Sci Technol 13:1164–1169
61. Zhu J, Zhou Y, Wu W, Deng Y, Xiang Y (2019) A novel rose-like CuS/Bi_2WO_6 composite for rhodamine B degradation. ChemistrySelect 4:11853–11861
62. Tarachand, Hussain S, Lalla NP, Kuo Y-K, Lakhani A, Sathe VG, Deshpande U, Okram GS (2018) Thermoelectric properties of Ag-doped CuS nanocomposites synthesized by a facile polyol method. Phys Chem Chem Phys 20:5926–5935
63. Wang C, Xu W, Xu C, Zhang Q, Zhang Z, Wang X, Fan Z, Xiong X (2022) Controlled synthesis of CuS-decorated CuO pillars over Cu mesh with improved wettability, photothermal and photocatalytic properties. J Mater Sci 57:15314–15330
64. Greenwood NN, Earnshaw A (1997) Chemistry of the Elements. Butterworth-Heinemann, Oxford
65. Saini S, Bargiela P, Fernandez V, Fairley N, Parvin S, Lee S, Weber J, McDowell MT, Baltrusaitis J (2025) Deriving stable peak models to fit complex XPS data from Cu contaminated Pt electrocatalysts. Surf Interface Anal 57:455–469
66. Khalakhan I, Vorokhta M, Xie X, Piliai L, Matolínová I (2021) On the interpretation of X-ray photoelectron spectra of Pt-Cu bimetallic alloys. J Electron Spectrosc Relat Phenom 246:147027
67. Chen X, Wang X, Fang D (2020) A review on C 1s XPS-spectra for some kinds of carbon materials. Fullerenes Nanotub Carbon Nanostruct 28:1048–1058
68. Batchelor-McAuley C (2023) Defining the onset potential. Curr Opin Electrochem 37:101176
69. Kumar M, Meena B, Subramanyam P, Suryakala D, Subrahmanyam C (2022) Recent trends in photoelectrochemical water splitting: the role of cocatalysts. NPG Asia Mater 14:88
70. Yang J, Wang D, Han H, Li C (2013) Roles of cocatalysts in photocatalysis and photoelectrocatalysis. Acc Chem Res 46:1900–1909
71. Kiliyankil VA, Mao W, Takahashi Y, Gong W, Kabayama S, Hamasaki Y, Fukutani K, Matsuzaki H, Sakata I, Takeuchi K, Endo M, Fugetsu B (2024) Edge sites on platinum electrocatalysts are responsible for discharge in the hydrogen evolution reaction. J Mater Chem A 12:28731–28743
72. Chantaramethakul J, Hussakan C, Yenmankhong Y, Chandeang P, Techapiesancharoenkij R, Hirunpinyopas W, Kasmui, Kurniawan C, Panomsuwan G (2024) Effect of carbon black supports on the hydrogen evolution reaction activity of Pd nanoparticle electrocatalysts synthesized via solution plasma sputtering. RSC Adv 14:31648–31654
73. Jiang P, Xiong Y, Xu M, Mei A, Sheng Y, Hong L, Jones TW, Wilson GJ, Xiong S, Li D, Hu Y, Rong Y, Han H (2018) The influence of the work function of hybrid carbon electrodes on printable mesoscopic perovskite solar cells. J Phys Chem C 122:16481–16487
74. Pantea D, Darmstadt H, Kaliaguine S, Roy C (2003) Electrical conductivity of conductive carbon blacks: influence of surface chemistry and topology. Appl Surf Sci 217:181–193
75. Auer E, Freund A, Pietsch J, Tacke T (1998) Carbons as supports for industrial precious metal catalysts. Appl Catal Gen 173:259–271
76. Morrison SR (1980) Electrochemistry at semiconductor and oxidized metal electrodes. Plenum Press, Nova York
77. Helander MG, Greiner MT, Wang ZB, Tang WM, Lu ZH (2011) Work function of fluorine doped tin oxide. J Vac Sci Technol A 29:011019
78. Michaelson HB (1977) The work function of the elements and its periodicity. J Appl Phys 48:4729–4733
79. Gerischer H (1977) On the stability of semiconductor electrodes against photodecomposition. J Electroanal Chem 82:133–143

80. Gerischer H (1978) Electrolytic decomposition and photodecomposition of compound semiconductors in contact with electrolytes. J Vac Sci Technol 15:1422–1425
81. Tan J, Kang B, Kim K, Kang D, Lee H, Ma S, Jang G, Lee H, Moon J (2022) Hydrogel protection strategy to stabilize water-splitting photoelectrodes. Nat Energy 7:537–547
82. Chawla SK, Sankarraman N, Payer JH (1922) Diagnostic spectra for XPS analysis of Cu-O-S-H compounds. J Electron Spectrosc Relat Phenom 61:1–18
83. Biesinger MC (2017) Advanced analysis of copper X-ray photoelectron spectra. Surf Interface Anal 49:1325–1334
84. Yang W, Moehl T, Service E, Tilley SD (2021) Operando analysis of semiconductor junctions in multi-layered photocathodes for solar water splitting by impedance spectroscopy. Adv Energy Mater 11:2003569
85. Gunawan M, Jin Y, Leung TC, Bowdler O, Zhou S, Gunawan D, Zhang M, Fang X, Zhang Q, Valanoor N, Amal R, Hart JN, Scott J, Toe CY (2025) Inducing n-type photoanodic behavior in p-type bismuth ferrite via ferroelectri
86. Formal FL, Tétreault N, Cornuz M, Moehl T, Grätzel M, Sivula K (2011) Passivating surface states on water splitting hematite photoanodes with alumina overlayers. Chem Sci 2:737–743